REVIEW

ADVANCED ELECTRONIC MATERIALS
www.advelectronicmat.de

XPEEM and MFM Imaging of Ferroic Materials

Massimo Ghidini, Francesco Maccherozzi, Sarnjeet S. Dhesi,* and Neil D. Mathur**

The authors describe and compare two complementary techniques that are habitually used to image ferromagnetic and ferroelectric materials with submicron spatial resolutions (typically 50 nm, at best 10 nm). The first technique is variable-temperature photoemission electron microscopy with magnetic/antiferromagnetic/polar contrast from circularly/linearly polarized incident X-rays (XPEEM). The second technique is magnetic force microscopy (MFM). Focusing mainly on the authors' own work, but not exclusively, published/unpublished XPEEM and MFM images of ferroic domains and complex magnetic textures (involving vortices and phase separation) are presented. Highlights include the use of two XPEEM images to create 2D vector maps of in-plane (IP) magnetization, and the use of imaging to detect electrically driven local reversals of magnetization. The brief and simple descriptions of XPEEM and MFM should be useful for beginners seeking to employ these techniques in order to understand and harness ferroic materials.

1. Imaging Ferroic Inhomogeneity

Spatial variations of magnetic and polar order can be exploited in the design of spintronic, ferroelectric, and magnetoelectric devices that store, process and read information.[1–5] However, scientific interest alone provides sufficient reason for imaging these types of spatial variation. The spatial variations of order parameter could arise in any samples with structural/chemical inhomogeneity,[6,7] in large samples due to the formation of ferroic domains,[1,8] in small samples due to defects and boundaries,[9] and in thin-film multilayers that support topological defects of magnetic[10–12] and polar[13,14] order. Topological defects include skyrmions and vortices (5–100 nm in diameter), which can be electrically/magnetically manipulated, and used to carry topologically protected information in memory and logic devices.[15,16]

XPEEM provides images of surface order down to a probe depth of several nanometers.[17] If the incident X-rays are circularly polarized then one can image a local magnetization, while if the incident X-rays are linearly polarized then one can also image antiferromagnetic order, or polar order such as ferroelectric domains.[18] Magnetic force microscopy (MFM) measures out-of-plane gradients of stray magnetic field.[19] Both techniques offer sub-micron spatial resolutions (typically 50 nm, at best 10 nm,[20,21]), which is highly desirable when imaging ferroic domain structures, and essential when imaging complex magnetic/antiferromagnetic/polar textures. In this paper, we explain the principles behind XPEEM and MFM, we compare the two techniques, and we present a range of XPEEM and MFM images. These images include XPEEM vector maps of magnetization, and MFM and XPEEM images that show local magnetoelectric effects.

The paper has 11 sections that include some very brief additions with respect to the topics described above. Section 2 outlines the principles of photoemission electron microscopy (PEEM). Section 3 describes topographical contrast and its relevance in the construction of magnetic vector maps. Section 4 explains how work function contrast can be used to distinguish ferroic domains. Both of these contrast mechanism can be achieved with UV light, thus demonstrating that there is some scope for PEEM experiments without synchrotron X-rays. Section 5 introduces synchrotron X-rays, which are used for chemical contrast (Section 6) and magnetic/polar contrast (Section 7). Section 7.1. covers X-ray magnetic circular dichroism (XMCD) due to a net magnetization. Section 7.2. covers X-ray linear dichroism (XLD), which arises due to anisotropic spin distributions (X-ray magnetic linear dichroism, XMLD) or anisotropic charge distributions (X-ray natural dichroism, XNLD). Section 8 describes MFM and distinguishes three different imaging modes. Section 9 compares XPEEM and MFM, and very briefly sets them in a more general context that recognizes the other methods for magnetic imaging. Section 10 shows how XPEEM and MFM can be used to image voltage-driven magnetic changes, which is extremely valuable in the study of magnetoelectrics, thus motivating our interest. Section 11 provides a summary and some comments on future developments.

The point of this paper is to provide beginners with a basic understanding of XPEEM and MFM. The XPEEM and MFM images that we show reflect our interest in ferroic materials and magnetoelectric effects in ferroelectric/ferromagnetic

M. Ghidini
Department of Mathematics
Physics and Computer Science
University of Parma
Parma 43124, Italy
E-mail: massimo.ghidini@unipr.it

M. Ghidini, F. Maccherozzi, S. S. Dhesi
Diamond Light Source
Chilton, Didcot, Oxfordshire OX11 0DE, UK
E-mail: dhesi@diamond.ac.uk

M. Ghidini, N. D. Mathur
Department of Materials Science
University of Cambridge
Cambridge CB3 0FS, UK
E-mail: ndm12@cam.ac.uk

The ORCID identification number(s) for the author(s) of this article can be found under https://doi.org/10.1002/aelm.202200162.

DOI: 10.1002/aelm.202200162

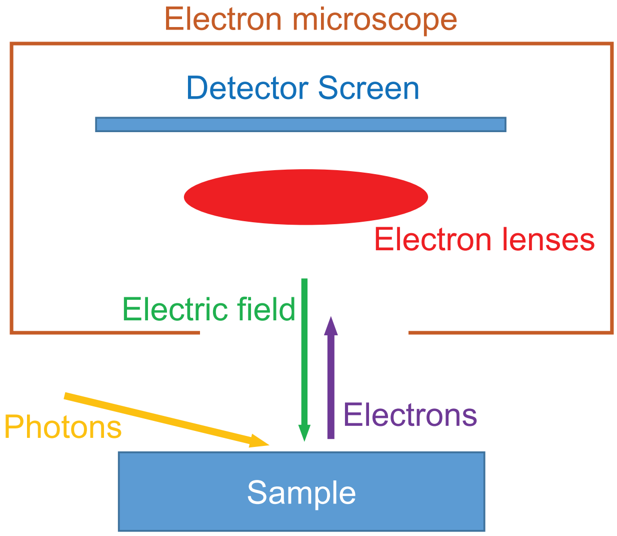

Figure 1. The working principle of PEEM. Photon absorption at the sample surface results in the emission of electrons. These electrons are accelerated by an electric field, and pass through magnetic and electrostatic lenses to form an intensity-absorption map on a detector screen.

heterostructures (rather than single-phase multiferroic materials). These images are primarily selected from our own published and unpublished work, which is thus to some extent reviewed. Given that this paper is not a comprehensive review, we have not cited many important works merely to include them in the reference list without explanation. We hope that this paper will inspire the imaginative use of XPEEM and MFM, and permit critical evaluation of literature.

2. PEEM

PEEM (**Figure 1**) requires i) reasonably conductive samples that include conducting films on insulating substrates and insulating films on conducting substrates; ii) suitable photon illumination of a given sample; iii) an accelerating electric field and electron lenses to collect the electrons that are thus emitted from near the sample surface; and iv) a detector screen to map the electron intensity emitted by the sample.

3. PEEM Images of Topography

Topographical contrast is obtained when surface features distort the local accelerating electric field, thus modifying the local intensity of electrons emitted in response to UV or X-ray illumination.[22] Although our interest has not focused on topographical contrast in its own right, topographical contrast has been essential when performing the alignment and distortion corrections that we required to construct magnetic vector maps from XPEEM images obtained with orthogonal sample orientations (see ref. [23] and later). Note that topographical images are not necessarily pure in light of the fact that contrast can also arise from the other mechanisms described in this paper (work function, chemistry, charge, magnetism).

4. PEEM Images of Work Function

One does not necessarily need synchrotron X-rays to form a PEEM image, as one can exploit the photoelectric effect using UV light from a mercury lamp or laser. The energy of the emitted electrons $h\nu - W$ is given by the energy of incident photons $h\nu$ less the sample work function W, which is thus mapped to yield work function contrast. Work function contrast can arise due to chemical inhomogeneity[17] or crystallographic orientation.[24] The latter contrast mechanism is relevant for ferroic materials, and has been exploited to image ferroelectric domains at a $BaTiO_3$ (BTO) surface.[25] If synchrotron X-rays are used instead of UV light then the emission of photoelectrons is dominated by secondary electron emission, permitting access to chemical, magnetic and structural images. As with topographical images, work function images are not necessarily pure.

5. Synchrotron X-Rays

Synchrotron X-ray beams are intense, highly collimated, tunable in energy, tunable in polarization, and pulsed. Combinations of these properties permit them to be employed to provide chemical, magnetic, and structural information for spectroscopy and imaging, which may be time-resolved by virtue of the pulsed nature of the beam. Synchrotron X-ray beams also facilitate experiments that exploit weak interactions, for example, X-ray magnetic scattering[26] and EXAFS.[27] As we will see, chemical contrast can be obtained in XPEEM by exploiting the tunable beam energy, while magnetic contrast is obtained by exploiting both the tunable beam energy and the tunable polarization. As we will see in what follows, the chemical and magnetic contrast is obtained from information carried by secondary electrons that escape from the sample. Escape requires these secondary electrons to be generated from within a few nanometers of the surface, such that the chemical and magnetic contrast represents the surface region only, even though X-rays penetrate much further. A common feature of synchrotron X-ray experiments is that the high intensity permits rapid acquisition of data, which can be averaged for good signal-to-noise ratios and thus good sensitivity.

6. Chemical Contrast with X-Ray Absorption Spectroscopy

Near-surface chemical contrast is achieved in a three-step X-ray absorption spectroscopy (XAS) process (**Figure 2**). The three-step process begins when the energy $h\nu$ associated with X-ray photons is tuned to excite electrons from core levels to empty states near the Fermi energy (Figure 2a). The resulting core holes are then filled by other electrons, in a process where energy is conserved not by photon emission but rather by the emission of Auger electrons with energies that contain chemical information (Figure 2b). The Auger electrons undergo inelastic scattering processes that generate secondary electrons (Figure 2c), whose intensity-energy distribution displays a relatively large peak when the X-ray photon energy is

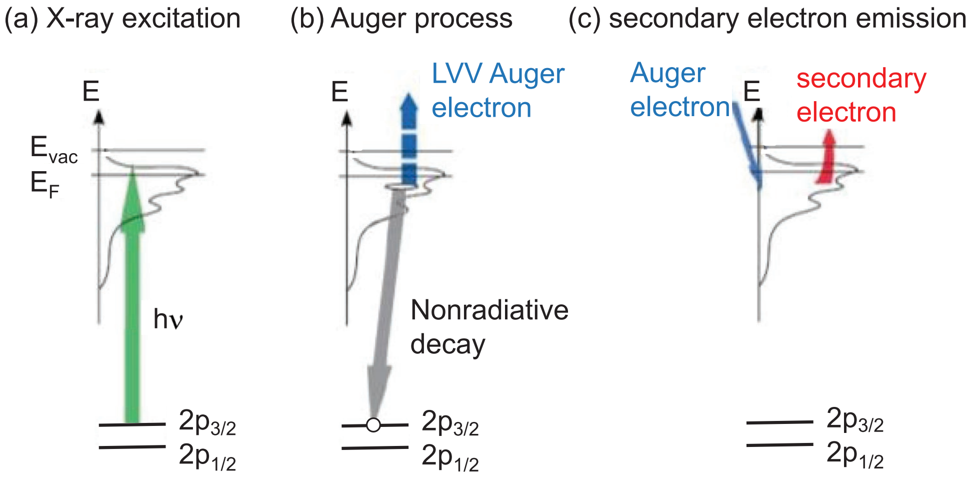

Figure 2. Chemical contrast via XAS. The three-step mechanism involves a) the promotion of core electrons to valence bands, b) the filling of the core holes via non-radiative decay coupled with the emission of Auger electrons, and c) secondary electron emission driven by inelastic scattering of Auger electrons. Reproduced with permission.[17] Copyright 2002, IOP Publishing. Note that Auger electrons are labeled with three capital letters: the first represents the shell of the hole, the second represents the shell of the electron that fills the hole, and the third represents the shell from which the Auger electron is emitted.[28] For the LVV Auger electrons in (b), L represents the shell of the 2p core hole, and V represents the valence band.

tuned to specific values that depend on, and thus reveal, the chemical species present. As with topographical images and work function images, chemical images are not necessarily pure.

An example of chemical contrast mapping is presented in **Figure 3**, where ferromagnetic dots of Ni (Figure 3b) and their ferroelectric substrate of BTO (Figure 3c) appear bright after tuning the photon energy to X-ray absorption edges for Ni and Ti, respectively. The images show the intensity of secondary electron emission, and we will adopt the standard practice of referring to this intensity as XAS intensity. XAS intensity data of the type shown here could be obtained with any X-ray polarization. Here the intensities measured with both left and right circularly polarized light were added together.

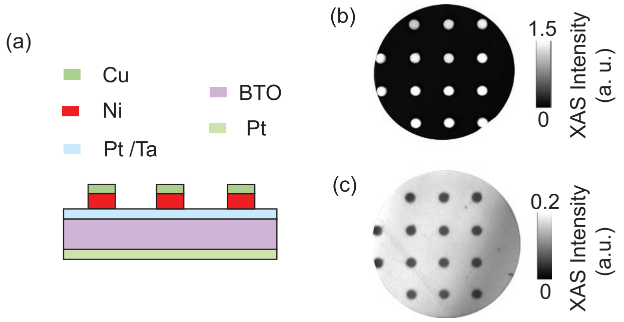

Figure 3. XAS-PEEM images with chemical contrast for a multiferroic heterostructure. a) Schematic showing Ni discs (diameter 1 µm, thickness 25 nm) on an electroded BTO substrate. The Ni discs have a Cu cap to avoid oxidation. The 2 nm-thick top electrode is thick enough to prevent charging during PEEM, and thin enough to permit the underlying BTO to be imaged. XAS-PEEM images obtained in the as-shown field of view (diameter 15 µm) reveal b) the Ni dots when using a photon energy (851 eV) that lies at the Ni L_3 absorption edge, and c) the BTO substrate when using a photon energy (457 eV) that lies at the Ti L_3 absorption edge. Reproduced with permission.[29] Copyright 2020, Royal Society of Chemistry.

7. Magnetic and Polar Contrast with XMCD and XLD

Ferroic materials are dichroic because the anisotropic distributions of spin and/or charge render X-ray absorption dependent on polarization, such that the resulting emission of near-surface secondary electrons (via the three-step near-surface process of Figure 2) is also dependent on polarization. For suitably oriented samples with a net magnetization, the difference in secondary electron emission arising from circularly polarized X-rays with opposite helicities yields magnetic contrast in spectroscopy and XPEEM imaging experiments, and the material is said to display XMCD. If instead, one employs linearly polarized X-rays with perpendicular polarizations then XLD can arise due to anisotropic spin distributions in antiferromagnets and uniaxial ferromagnets/ferrimagnets (XMLD) or anisotropic charge distributions in polar materials (XNLD). We will show in the following

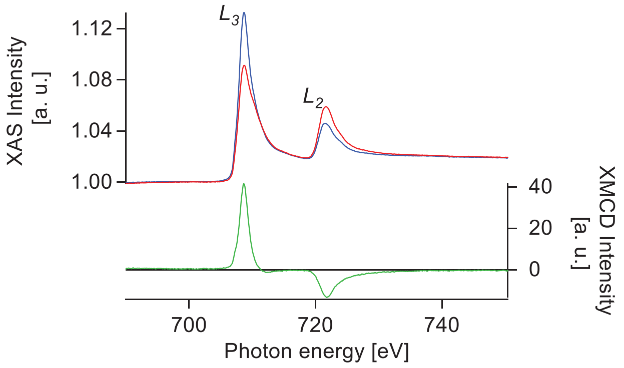

Figure 4. Spectroscopic XMCD data for an iron film. XAS intensity arising from secondary electron emission due to circularly polarized light of negative (blue) and positive (red) helicity. The difference yields the XMCD intensity (green), which deviates from zero near the L_3 and L_2 absorption edges. The iron is single domain due to the application of 0.5 T in a direction that lies parallel to the IP projection of the X-ray beam, whose angle of incidence is less than 90°.

sub-sections how one may thus employ XMCD contrast to study ferromagnets, XMLD contrast to study antiferromagnets, and XNLD contrast to study ferroelectrics. In XPEEM images, these near-surface contrast mechanisms reveal any ferroic domains. Magnetic/polar contrast obtained with a single helicity/polarization is necessarily impure, but is highly purified by dichroism.

7.1. XMCD

XMCD exploits circularly polarized X-rays, whose photons carry spin angular momentum. If this angular momentum (+ħ) lies parallel to the wave propagation vector ***k*** then one has positive (+) helicity or right (R) circular polarization, while in the antiparallel scenario (-ħ) one has negative (-) helicity or left (L) circular polarization. Equally, when the ray is viewed from the perspective of an observer toward whom the ray is traveling, the electric vector **E** of R-polarized (L-polarized) light rotates counterclockwise (clockwise) within a fixed plane that lies perpendicular to the ray direction.

Spectroscopic XMCD data for ferromagnetic iron are presented in **Figure 4**. The secondary electron emission (XAS intensity) that follows the absorption of X-rays with opposite helicities is polarization-dependent near the L_3 and L_2 absorption edges (red and blue data, Figure 4). The difference between these two plots yields the XMCD intensity (green data, Figure 4), whose magnitude is proportional to the magnitude of the surface magnetization component that lies parallel to the grazing-incidence X-ray beam, and whose sign is different for the L_3 and L_2 edges.

The XMCD spectrum in Figure 4 may be understood in terms of the L_3 ($2p_{3/2} \rightarrow 3d$) and L_2 ($2p_{1/2} \rightarrow 3d$) absorption edges for electronic transitions from the 2p core levels to the 3d valence band (**Figure** 5a,b) ($2p_{3/2}$ has positive spin-orbit coupling such that $J = L + S = 3/2$, $2p_{1/2}$ has negative spin-orbit coupling such that $J = L - S = 1/2$). First, we observe that the ≈10 eV separation of these two edges is due to the spin-orbit splitting of the $2p_{3/2}$ and $2p_{1/2}$ levels. Second, we observe that the L_3 peaks are more intense than L_2 peaks because the $2p_{3/2}$ level contains twice as many states as the $2p_{1/2}$ level. Third, we may understand the XMCD contrast of interest via the following two-step model,[18] assuming that the photons with positive (Figure 5a) and negative (Figure 5b) helicity impinge upon a material with positive magnetization (Figure 5a,b). The two steps are reminiscent of spatially separated sequential processes in spintronic devices,[30] but here their separation is conceptual and they describe single-step quantum-mechanical transitions.

1. First step: Spin polarization. Electrons excited from the $2p_{3/2}$ and $2p_{1/2}$ levels possess net spin polarizations of opposite sign (red arrows in Figure 5) due to conservation of angular momentum and spin-orbit coupling. Specifically, photons with positive (negative) helicity transfer a positive (negative) orbital angular momentum to 2p electrons, such that $2p_{3/2}$ electrons with L parallel to S develop a net spin-up (spin-down) polarization, while $2p_{1/2}$ electrons with L antiparallel to S develop a net spin-down (spin-up) polarization.
2. Second step: d-band spin filtering. The spin-polarized 3d band represents a spin filter for the spin-polarized photoelectrons. This is because the spin-dependent density of empty states near the Fermi energy determines the probability of the $2p \rightarrow 3d$ transitions, and thus the intensity of the corresponding absorption peak. Specifically, for photons with positive (negative) helicity, the $2p_{3/2}$ electrons promoted with a net spin-up (spin-down) polarization have access to more (fewer) empty states near the Fermi energy and so the intensity of the L_3 absorption peak is larger (smaller), while the $2p_{1/2}$ electrons promoted with a net spin-down (spin-up) polarization have access to fewer (more) empty states near the Fermi energy and so the intensity of the L_2 absorption peak is smaller (larger).

In the above example and elsewhere, a reversal of magnetization reverses the relative magnitudes of the XAS intensities at each absorption edge, thus switching the sign of the XMCD intensity. More generally, the XMCD intensity at a given absorption edge depends on the angle between the surface magnetization **M** and the photon angular momentum, whose alignment (anti-alignment) for positive (negative) helicity with beam wavevector **k** implies that the XMCD intensity at a given absorption edge is proportional to the dot product **M.k**, and the

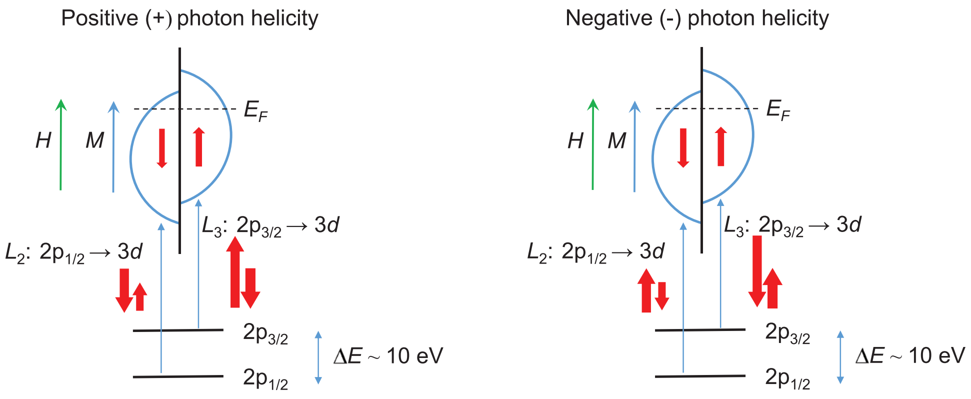

Figure 5. The principle of XMCD. Circularly polarized X-rays excite spin-polarized electrons from the $2p_{1/2}$ and $2p_{3/2}$ core levels with net spin polarizations of opposite sign due to opposite-sign spin-orbit coupling. Red arrow directions represent spin orientations, red arrow lengths represent photoelectron populations. An applied magnetic field H can be used to set and enhance the magnetization M, which in both (a) and (b) lies parallel to the IP projection of the X-ray beam, whose angle of incidence is less than 90°.

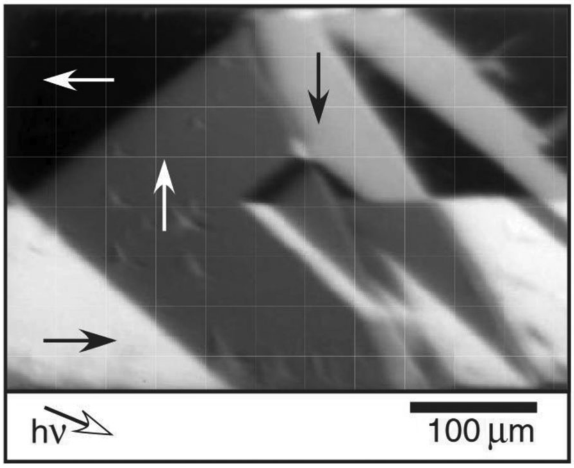

Figure 6. XMCD-PEEM image of IP magnetic domains in an Fe (001) whisker. Four directions of magnetization are identified using arrows. If the IP projection of the grazing-incidence beam (bottom arrow) were perfectly aligned with the magnetization of the white domain then the grey domains (vertical arrows) would display exactly the same contrast. The greyscale for magnetic contrast is absent. Reproduced with permission.[17] Copyright 2002, IOP Publishing.

sign of the proportionality constant depends on the choice of absorption edge. The XMCD intensity at a given absorption edge therefore measures the component of surface magnetization parallel or anti-parallel to the fixed beam direction. The X-ray beam typically impinges with an angle of incidence that is less than 90° on a surface region where the magnetization lies wholly in plane. XMCD intensity at a given absorption edge can then be read with sign to identify whether the surface magnetization lies parallel (maximum value), antiparallel (minimum value), perpendicular (zero), or otherwise (intermediate value) with respect to the IP component of the beam direction. Note that in both spectroscopy and imaging experiments, instead of establishing the difference between XAS intensities measured with R and L helicities, the XAS intensity for a single helicity is sometimes reported in lieu of XMCD intensity (e.g., if it is difficult to change X-ray polarization). This experimental simplification is reasonable in scenarios where it makes little difference to effect the subtraction.

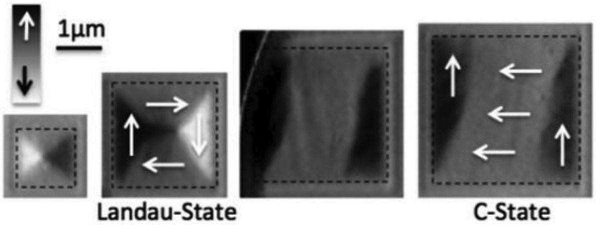

Figure 7. XMCD-PEEM images of IP magnetic domains in a patterned $La_{0.7}Sr_{0.3}MnO_3$ film. Directions of magnetization are identified using arrows. The second image displays Landau flux-closure domains, and the last image displays a C-state. The IP projection of the grazing-incidence beam (up on the page, see greyscale top-left) is well aligned with the magnetization of the black domain. Black dashes bound the patterned $La_{0.7}Sr_{0.3}MnO_3$ squares of thickness 15 nm. Reproduced with permission.[32] Copyright 2011, American Institute of Physics.

7.1.1. XMCD-PEEM Images

We have seen that an XMCD spectrum may be constructed by subtracting two XAS spectra that were obtained with photons of opposite helicity (Figure 4). Instead of collecting each of these XAS spectra at different X-ray photon energies, one may obtain an XAS-PEEM image at some absorption edge. Pixel-by-pixel subtraction of the two XAS-PEEM images yields an XMCD-PEEM image that maps XMCD intensity at the absorption edge. The subtraction is employed because it enhances magnetic contrast by eliminating non-magnetic contrast, perfectly or imperfectly in practice. One can eliminate the unwanted effect of inhomogeneous X-ray illumination by dividing the difference of XAS intensities by their sum to yield XMCD asymmetry, or by comparing XAS intensities at the absorption edge with XAS intensities away from the absorption edge (described more compactly as on and off resonance).[31] An XMCD-PEEM image might typically map XMCD asymmetry at the absorption edge, which as explained in the previous paragraph for XMCD intensity, represents the projection of the local surface magnetization onto the beam direction. An XMCD-PEEM image thus constitutes a map of local magnetization, and the signal-to-noise ratio for each pixel will be improved by averaging data from many XMCD-PEEM images.

Let us consider an XMCD-PEEM image of magnetic domains that lie in the plane of the sample surface (**Figure 6**). Domains whose magnetizations are roughly aligned/anti-aligned/perpendicular with IP projection of the beam appear white/black/grey. The two 90° domains are slightly different shades of grey because the IP projection of the beam (arrowed at the bottom of Figure 6) is not exactly perpendicular to their magnetization directions.

XMCD-PEEM images provide imperfect information about the local magnetization in two respects. First, the angle between the local magnetization and the IP projection of the beam can only in general be well resolved if the XMCD asymmetry is calibrated by rotating the sample about its surface normal. Second,

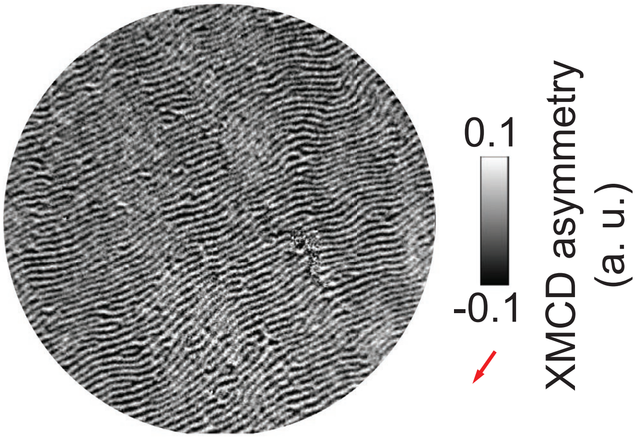

Figure 8. XMCD-PEEM image of an alternating OOP magnetization. Weak stripe domains in a 100 nm-thick film of Ni. The OOP component of magnetization alternates in sign, and it has a non-zero projection on the grazing-incidence beam, whose IP projection is arrowed. The relatively large IP component of magnetization lies orthogonal to the beam. Similar data are published in ref. [33]. Field of view diameter = 15 µm.

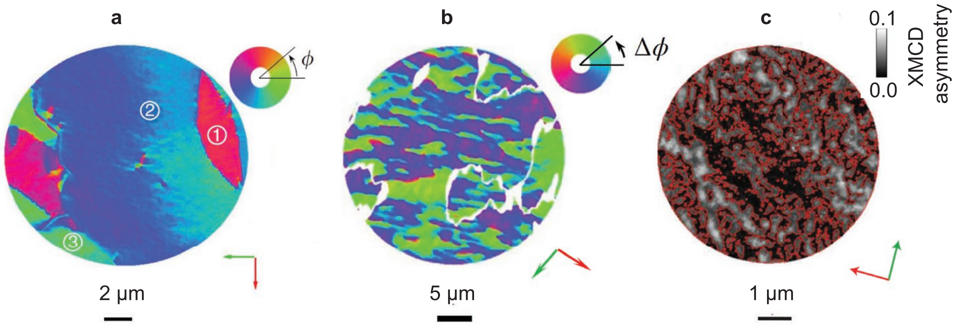

Figure 9. Visualization of complex magnetic microstructures. All images are based on XMCD-PEEM vector maps of magnetization that combine two XMCD-PEEM images obtained with orthogonal IP projections of the grazing-incidence beam (red and green arrows). a) XMCD-PEEM vector map of magnetization for a $La_{0.7}Sr_{0.3}MnO_3$ film that was grown epitaxially and transferred to an electroactive substrate on which it does not grow well. Color wheel identifies the direction of local magnetization. Reproduced with permission.[34] Copyright 2020, Springer Nature. b) Difference image obtained by subtracting XMCD-PEEM vector maps of a polycrystalline Ni film before and after ferroelectric domain switching in its electroactive substrate. Color wheel identifies changes in the direction of local magnetization. Reproduced with permission.[23] Copyright 2019, Springer Nature. c) The magnitude of the XMCD asymmetry for an XMCD-PEEM vector map of an $La_{0.7}Ca_{0.3}MnO_3$ film on a BTO substrate, at 210 K. Red contours enclose black regions that are considered to possess zero magnetization within error. Reproduced with permission.[35] Copyright 2013, Springer Nature.

one cannot know the sign of any magnetization component that lies perpendicular to the grazing-incidence beam (or equally its IP projection). This second point reveals that the magnetization directions marked on the XMCD-PEEM image in Figure 6 were partially identified via knowledge of Landau flux-closure domains; for example, the black arrow on the white domain was set at ≈45° to the domain wall that it points toward, thus determining the unmeasured sign of the component that lies perpendicular to the grazing-incidence beam (or equally its IP projection). If the IP projection of the grazing-incidence beam is collinear with respect to domains that appear black and white (**Figure 7**) then knowledge of Landau flux closure domains permits one to identify the magnetization directions for the intervening domains that appear to be a similar shade of grey, that is, one ensures head-to-tail arrangements.

XMCD-PEEM images will also be affected by any out-of-plane (OOP) components of magnetization, which have small projections on a grazing-incidence X-ray beam. We have imaged OOP components of magnetization by using a Ni film in which large IP components of magnetization are accompanied by an OOP component that alternates between up and down to form weak stripe domains (**Figure 8**) (locally, the IP component of magnetization lies parallel to the stripe direction). Given that the projection of OOP components of magnetization on the grazing-incidence beam is unaffected by IP sample orientation, stripe domains are visible for any IP sample orientation.[33]

7.1.2. XMCD-PEEM Vector Maps

In order to identify IP magnetization directions accurately and unambiguously, we habitually combine pairs of XMCD-PEEM images to construct vector maps of IP magnetization (vector addition of orthogonal IP magnetization components, details in, e.g., ref. [34]). Any regions with an OOP magnetization component should be excluded, but Bloch walls can be tolerated even if they are resolved, as Bloch wall locations will be apparent from the IP domains that they separate. Vector maps and their derivatives permit the visualization of complex magnetic microstructures (**Figure 9**), thus providing great insight into physical phenomena of interest. For example, the vector map in Figure 9a was relevant in a magnetoelectric study where magnetic domain walls were found to be associated with cracks in a transferred film;[34] the difference between two vector maps (Figure 9b) was relevant in a magnetoelectric study where non-orthogonal IP magnetic switching in a film revealed a hitherto ignored shear strain associated with ferroelectric domain switching in a substrate of PMN-PT ($0.7Pb(Mg_{1/3}Nb_{2/3})O_3$–$0.3PbTiO_3$);[23] and the magnitude of the local magnetization (Figure 9c) was evaluated from a vector map and used to help reveal that extrinsic magnetocaloric effects are associated with the observed phase separation.[35] Magnetic vector maps are rare in the literature, but an XMLD-PEEM vector map appears later in Figure 19.

Figure 10 demonstrates the creation of a vector map from two XMCD-PEEM images, which are challenging to read individually. The two individual XMCD-PEEM images (Figure 10a,b) are

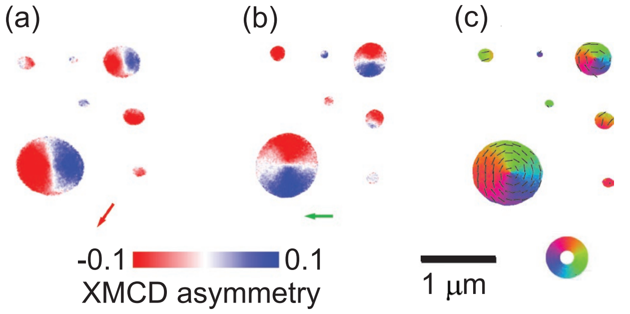

Figure 10. XMCD-PEEM images and vector maps of vortex magnetization. For seven CoFeB discs of diameter 100 nm–2 µm, we show a,b) XMCD-PEEM images obtained with the IP projection of the grazing-incidence beam aligned with the a) red and b) green arrows, that is, orthogonally. c) The resulting magnetic vector map reveals the vortex state via the color wheel and arrows, both of which show the direction of IP magnetization. Sample details are similar to those shown in Figure 3a schematic, where all discs have the same diameter.

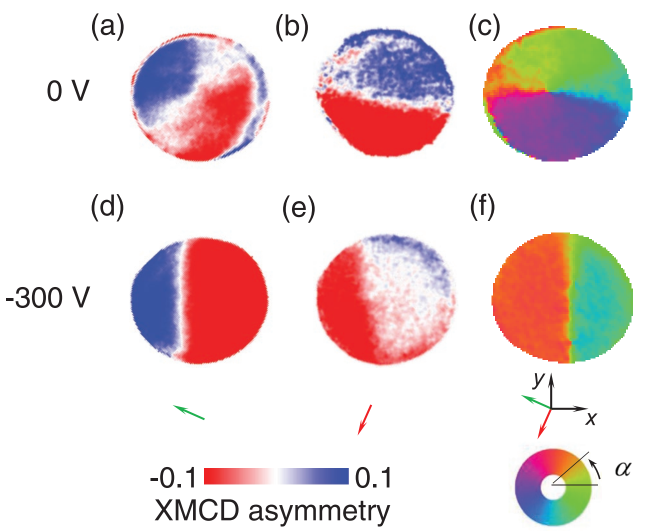

Figure 11. XMCD-PEEM images and vector maps of anisotropic vortex magnetization. For a Ni disc of diameter 1 µm, we show a,b) XMCD-PEEM images obtained with the IP projection of the grazing-incidence beam aligned with the a) green and b) red arrows, that is, orthogonally. c) The resulting magnetic vector map reveals the vortex state via the color wheel, which shows the direction of IP magnetization. Panels (d–f) show the corresponding data with −300 V across the electroded BTO substrate. Figure 3a shows a schematic of the sample that contained the imaged disc. Reproduced with permission.[29] Copyright 2017, Royal Society of Chemistry.

obtained with the sample rotated 90° about the surface normal, and the two images are presented for ease of visualization with the sample in a single orientation and the IP projection of the beam rotated by 90°. Note that the combination of the two XMCD-PEEM images involves correcting for drift and distortion via topographical information (e.g., specks of dirt) from the XAS-PEEM images that are subtracted to yield the XMCD-PEEM images.

If one considers Figure 10a or Figure 10b alone, it would be most natural to conclude that the two largest magnetic discs comprise anti-parallel bi-domains on either side of a domain wall. However, the vector map in Figure 10c reveals that these discs contain a magnetic vortex. The value of the vector map is even greater if the vortex state is anisotropic (**Figure 11**a–c). The individual XMCD-PEEM images (Figure 11a,b) might well appear to represent anti-parallel bi-domains on either side of a domain wall, but the resulting vector map (Figure 11c) reveals that the horizontally running "wall" has opposite chiralities on either side of the disc center. For comparison, we present data for anti-parallel bi-domains in the same disc after voltage-induced strain from an electroactive substrate (Figure 11d–f).

7.2. XLD

XLD exploits linearly polarized X-rays, with mutually perpendicular polarizations that can be described in two ways. First, one may refer to polarizations that are vertical (V) and horizontal (H) with respect to the sample surface, assuming a beam whose angle of incidence is less than 90°, and inaccurately using "vertical" to describe off-vertical. Second, one may refer to polarizations that are parallel (||) and perpendicular (⊥) to some anisotropic direction in the material under study. The difference between XAS intensity data obtained with two orthogonal polarizations then yields XLD contrast in spectroscopy and imaging experiments, most notably at *L* absorption edges, thus providing chemical sensitivity.

The linearly polarized photons carry no angular momentum, and XLD intensity arises due to anisotropic distributions of charge. One may refer to X-ray Linear Natural Dichroism (XNLD) intensity when the charge anisotropy is associated with chemical bonding, for example, in ferroelectrics. Alternatively, one may refer to XMLD intensity when the charge anisotropy is associated with magnetism via spin-orbit coupling, for example, in antiferromagnets and uniaxial ferromagnets/ferrimagnets. Ferroelectric domains can thus be imaged using XNLD-PEEM, and antiferromagnetic domains can thus be imaged using XMLD-PEEM. Elsewhere, the terms XLD, XNLD, and XMLD are used somewhat interchangeably.

Note that in both spectroscopy and imaging experiments, instead of establishing the difference between XAS intensities measured with perpendicular X-ray polarizations, the

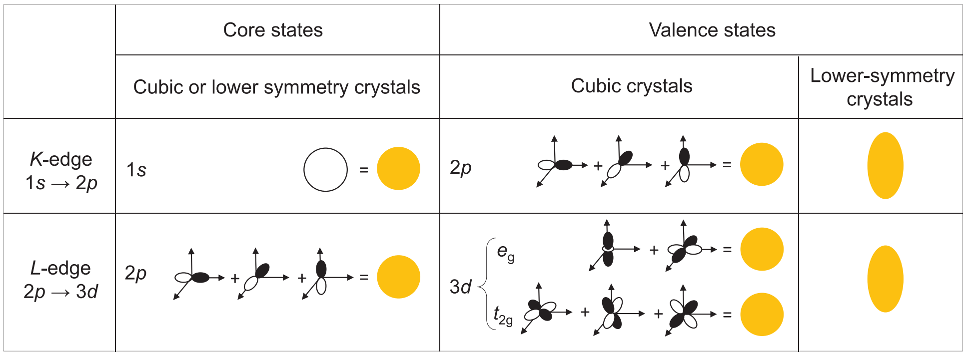

Figure 12. Origin of XNLD. The cartoon describes K-edge (1s → 2p) and L-edge (2p → 3d) transitions in a non-magnetic crystal of cubic or lower symmetry. The fully occupied degenerate core states from which electrons are excited yield spherically symmetric charge distributions (yellow discs) in both cubic and lower symmetries. In cubic symmetry, the degenerate valence states to which electrons are excited yield spherically symmetric charge distributions (yellow discs) in which the density of available states does not depend on orientation, such that XAS intensity is independent of the X-ray polarization direction. In lower symmetries, the valence states to which electrons are excited yield anisotropic charge distributions (schematized as yellow ellipses) in which the density of available states depends on orientation, such that XAS intensity depends on the X-ray polarization direction.

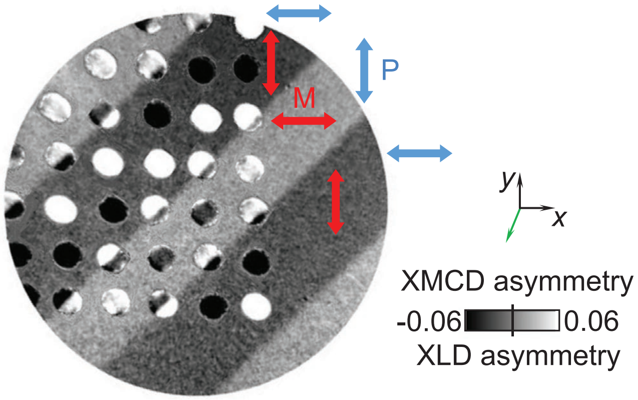

Figure 13. Image of ferroelectric and ferromagnetic domains. XMCD-PEEM image of polycrystalline Ni discs and the corresponding XLD-PEEM image of the surrounding BTO $(001)_{pc}$ substrate (pc denotes pseudocubic). For each ferroelectric domain, double-headed arrows show the axes of BTO polarization **P** (blue) and Ni magnetization **M** (red). Sample cross-section appears in Figure 3a, field of view has diameter 20 µm, green arrow represents IP projection of incident beam. Reproduced with permission.[39] Copyright 2018, IOP Publishing.

XAS intensity for a single polarization is sometimes reported in lieu of XLD intensity (e.g., if it is difficult to change X-ray polarization). This experimental simplification is reasonable in scenarios where it makes little difference to effect the subtraction. The XLD, XNLD, and XMLD intensities evaluated in this way are proportional to the square of the cosine of the angle between the single X-ray polarization and the symmetry axis, while the XMLD intensities evaluated in this way are also proportional to the square of the local magnetization (which is finite in antiferromagnets).[18]

7.2.1. XNLD

Non-magnetic materials display XNLD if the valence orbitals around the absorbing atoms are anisotropic, for example, in non-centrosymmetric ferroelectric domains.[36,37] The secondary electron emission that gives rise to XNLD intensity is proportional to the intensity of K-edge (1s → 2p) and L-edge (2p → 3d) transitions that take place from spherically symmetric filled (core) states to available (valence) states that are anisotropic if the symmetry is lower than cubic (**Figure 12**). Anisotropic valence states imply anisotropic absorption and thus anisotropic secondary electron emission. The linearly polarized X-ray beam thus represents a "search light" by analogy with an electric torch whose beam is swept around some scene of interest.[37,18]

7.2.2. XNLD-PEEM Images

Ferroelectric domains in single crystals of tetragonal BTO have been revealed via XNLD-PEEM images that were obtained at the Ti L_3 edge.[33,38] The electrical polarization of the pseudocubic unit cell lies parallel to the *c* lattice parameter, and perpendicular to the two *a* lattice parameters that are 1% smaller than the *c* lattice parameter. A pseudocubic (001) surface can thus present *c* domains in which the *c* lattice parameter and polarization are oriented OOP (up or down), or *a* domains in which an *a* lattice parameter is oriented OOP and the polarization is oriented along one of the four IP pseudocubic <100> directions.

If voltage-driven 90° domain switching in BTO interconverts *a* and *c* domains at a pseudocubic (001) surface then the resulting uniaxial strains of ±1% can be transferred to the corresponding region of say an overlying Ni film in which there are magnetic changes via magnetostriction. We have studied this

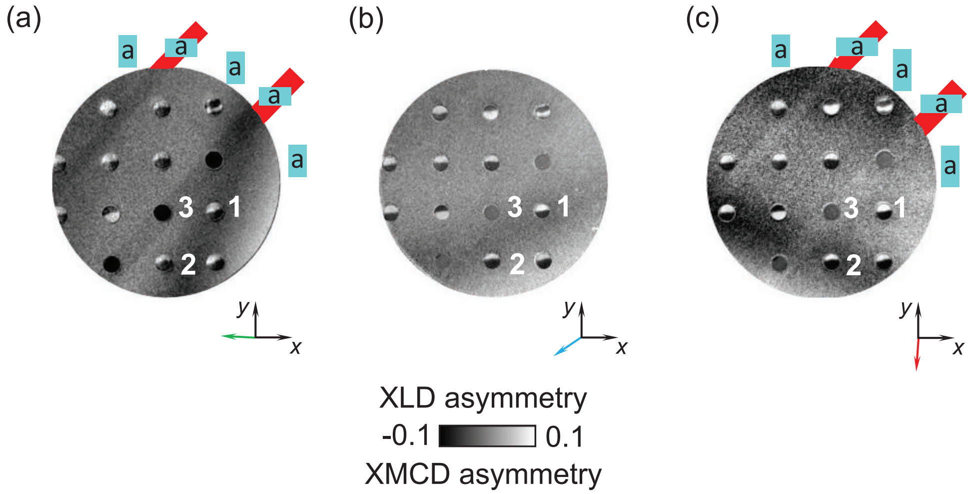

Figure 14. Images of ferroelectric and ferromagnetic domains for different IP sample orientations. For each panel, the XMCD-PEEM image of polycrystalline Ni discs, and the corresponding XLD-PEEM image of the surrounding BTO $(001)_{pc}$ substrate (pc denotes pseudocubic), were both obtained with the IP projection of grazing-incidence beam parallel to the a) green, b) blue and c) red arrows. The perception of ferroelectric BTO domains in (a,c) and not (b) implies that the 30 µm-diameter field of view exclusively contains *a* domains, whose unit cells are represented by the blue rectangles ($c > a$). Red strips that extrapolate one species of *a* domain are a guide to the eye. Sample cross-section appears in Figure 3a. Reproduced with permission.[40] Copyright 2020, IOP Publishing.

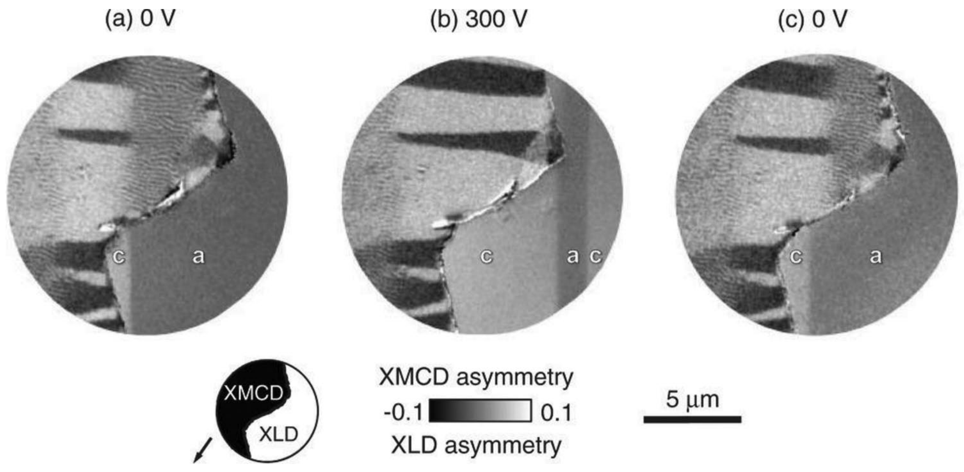

Figure 15. Images of ferroelectric (ferromagnetic) domains that mediate (manifest) magnetoelectric effects. For voltages of 0, 300, and 0 V that were applied between a polycrystalline Ni film and an electrode under its BTO $(001)_{pc}$ substrate (pc denotes pseudocubic), we show XMCD-PEEM images of the film and the corresponding XLD-PEEM images of the substrate, near the jagged edge of a hole in the film. The as-marked *a* and *c* domains in the substrate were created following an electrical cycle prior to measurement, and by assuming that the exposed ferroelectric domains continue under the film, it can be seen that the voltage-driven changes in the substrate result in the reversible annihilation of weak stripe domains (grey areas with texture) in favor of IP magnetic domains (black and white). Arrow represents IP projection of incident beam. Reproduced with permission.[33] Copyright 2015, Wiley-VCH.

type of strain-mediated magnetoelectric effect using patterned films of polycrystalline Ni, such that regions of the BTO surface without Ni were only covered by the very thin top electrode (Figure 3) in order to permit XNLD-PEEM imaging. We then used XMCD-PEEM at the Ni L_3 edge to image ferromagnetic domain switching in Ni discs, and XNLD-PEEM at the Ti L_3 edge to observe nearby ferroelectric domain switching in the BTO substrate (**Figure 13**). By obtaining XNLD-PEEM images of such a BTO substrate at different IP orientations, it was possible to confirm that the surface in the field of view comprised *a* domains only (**Figure 14**). **Figure 15** presents images of both ferromagnetic and ferroelectric domains while different voltages were applied across the BTO substrate. Here there was a Ni film with holes instead of Ni discs. Part of one hole appears in the field of view. The Ni film was thick enough to display weak stripe domains, and these stripe domains were reversibly annihilated by the voltage-driven switching of underlying BTO domains.

7.2.3. XMLD

XMLD contrast has been widely employed in the spectroscopic study of magnetic materials.[41–43] If a spin axis is well defined then spin-orbit coupling results in a charge anisotropy that creates a difference in XAS intensities for parallel and perpendicular polarizations of a suitably oriented X-ray beam (**Figure 16**). The XMLD intensity is given by the difference of XAS intensities, or the XAS intensity for a single polarization.

7.2.4. XMLD-PEEM Images

XMLD-PEEM images are analogous to XMCD-PEEM images, and in this sub-section, we present images of antiferromagnetic domains, where brighter regions are better aligned with the single IP polarization that was employed. **Figure 17** shows antiferromagnetic domains in NiO. **Figure 18**a shows what may be regarded as an XMLD-PEEM image of antiferromagnetic domains in an epitaxial $LaFeO_3$ film, while Figure 18b shows what may be regarded as an XMCD-PEEM image of ferromagnetic domains in an ultra-thin overlayer of exchange-biased Co, thus

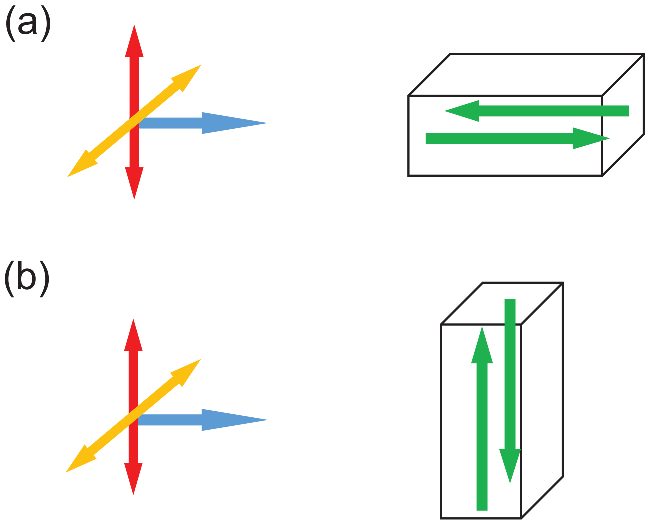

Figure 16. Schematic for XMLD in an antiferromagnet. a,b) The blue arrow denotes the direction of linearly polarized X-rays that are incident upon the sample with one of two orthogonal polarizations (red and yellow arrows). The sample is represented by just two localized spins (green arrows) that render the local charge distribution anisotropic via spin-orbit coupling. a) Both polarizations lie orthogonal to the spin axis, so the XAS intensities are the same, resulting in no XMLD contrast. b) One polarization lies orthogonal to the spin axis while the other lies parallel, so the XAS intensities are different, resulting in XMLD intensity.

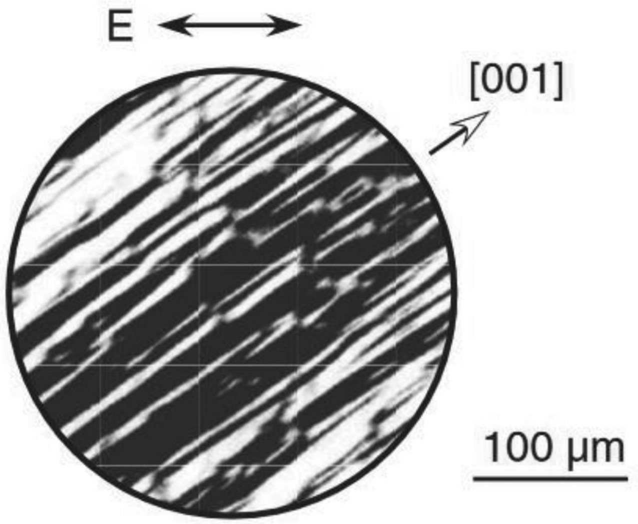

Figure 17. XMLD-PEEM image of antiferromagnetic domains in NiO. In brighter regions, the spin axis is better aligned with single beam polarization employed (double-headed arrow). Reproduced with permission.[17] Copyright 2002, IOP Publishing.

demonstrating that PEEM can be used to image different types of magnetic order in different layers of the same sample (the XPEEM images and XAS spectra in Figure 18 were obtained with a single X-ray polarization/helicity). **Figure 19** shows an XMLD-PEEM vector map of antiferromagnetic domains, where good angular resolution was required in practice.

8. MFM

MFM is a form of scanning force microscopy in which the cantilever tip is coated with a magnetic material that is essentially magnetized in the vertical direction, either up or down. The vertically vibrating tip repeats each topographical scan at a fixed lift height (e.g., 20–100 nm), where it is sensitive to suitably inhomogeneous stray magnetic fields from a suitable sample (not, therefore, an antiferromagnet). MFM contrast is identified via changes in the resonance frequency or phase of the vibrating cantilever. The magnetic dipolar forces on the vertically vibrating tip are proportional to the second derivative of the OOP stray field component with respect to vertical position. Although sample magnetization is therefore not directly mapped by MFM, it can readily be iden-

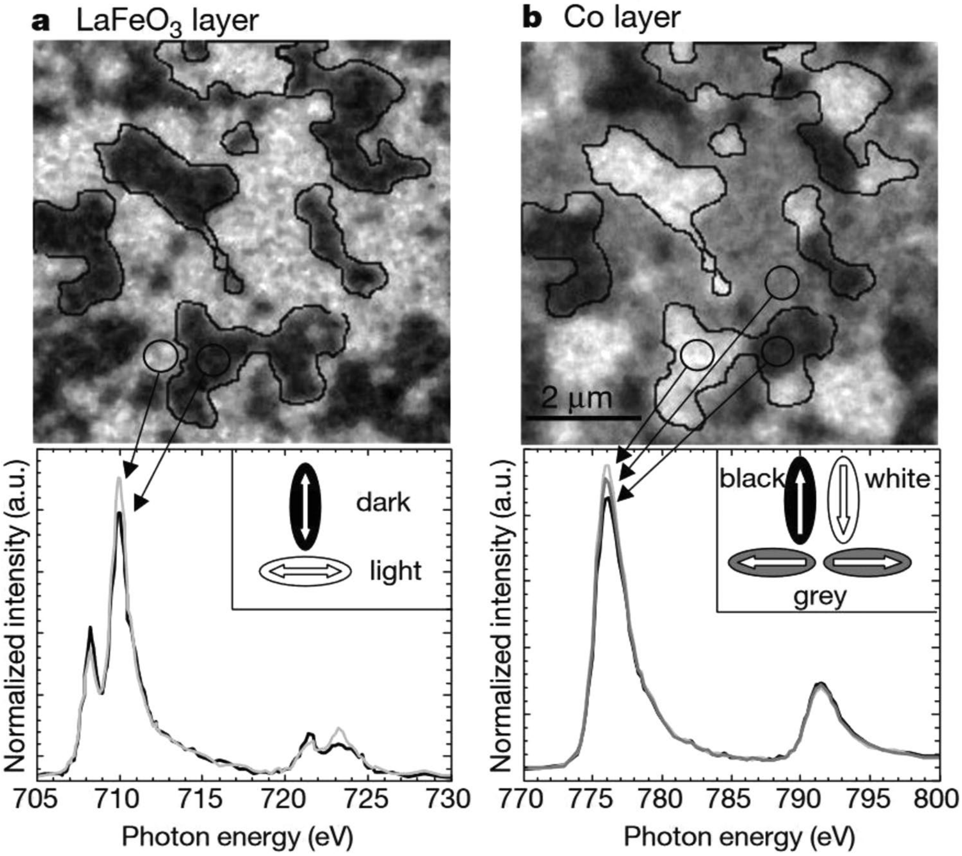

Figure 18. XPEEM images and XAS spectra of ferroic order in each component of a $LaFeO_3$/Co bilayer. a) XPEEM image obtained with a single X-ray polarization at the Fe L_3 edge revealing antiferromagnetic domains in an epitaxial film of $LaFeO_3$ grown on $SrTiO_3$ (001), and the corresponding XAS spectra for the two circled areas. b) XPEEM image obtained with a single X-ray helicity at the Co L_3 edge revealing ferromagnetic domains in a 1.2 nm-thick overlayer of Co, and the corresponding XAS spectra for the three circled areas. The IP projection of the beam direction runs vertically with respect to the figure. Subtraction of data obtained with different X-ray helicities (polarizations) would have yielded XMCD-PEEM images and XMCD spectra (XMLD-PEEM images and XMLD spectra). Reproduced with permission.[44] Copyright 2000, Springer Nature.

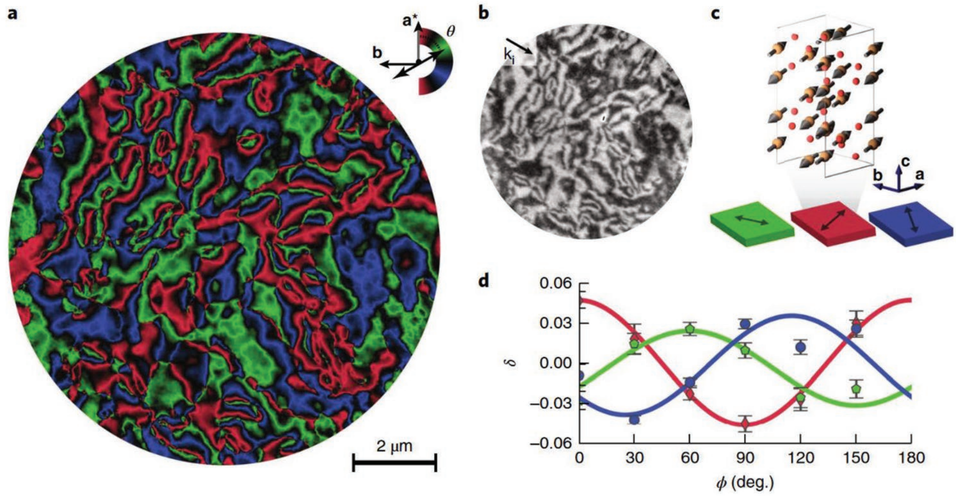

Figure 19. XMLD-PEEM vector map of α-Fe_2O_3. a) Vector map showing antiferromagnetic domains whose three spin axes are indicated by the color wheel. b) Single XMLD-PEEM image. In brighter regions, the spin axis is better aligned with single beam polarization employed. c) Crystal structure (top) and visualization of the three spin axes (bottom). d) XMLD contrast obtained for six IP sample orientations that were used to construct the vector map. Reproduced with permission.[45] Copyright 2018, Springer Nature.

tified for simple magnetic microstructures (e.g., a uniformly magnetized disc), and can otherwise be deduced via modeling. The lateral spatial resolution corresponds roughly to the lift height.

One should ensure that MFM signals arise due to magnetic dipolar forces only, and that tips are not exposed to electric fields that are liable to result in electrostatic forces, for example, during magnetoelectric measurements. Ideally, the sample would influence the vibration of an MFM tip whose magnetization is unaltered. Unfortunately, dipolar tip-sample interactions can sometimes be strong enough to modify the magnetization of the tip, the sample, or both; and three regimes involving weak, intermediate, and strong tip-sample interactions can be identified as follows.[1]

8.1. Charge Contrast

This is the optimal regime, in which the tip and sample interact without one modifying the magnetic configuration of the other, for example, when imaging a magnetic hard disc or recording tape with a tip of standard coercivity (**Figure 20**). The contrast can be understood using a magnetic charge model, where the magnetic force felt by the tip at a given location can be repulsive (bright) or attractive (dark) according to the relative polarities of tip magnetization and sample stray field.

8.2. Susceptibility Contrast

If dipolar tip-sample interactions cause the tip to reversibly modify the magnetic structure of the sample, or vice versa, then one of the tip and sample is "susceptible" to the other, and the resulting susceptibility contrast can reveal the magnetic configuration of the sample. For example, an attractive interaction in which the tip modifies the sample leads to contrast that is dark not bright, and the variations in dark contrast can be sufficient to reveal the magnetic configuration of the sample (**Figure 21**). In Figure 21, susceptibility contrast is confirmed by the observation that increasing the tip moment (thicker magnetic coating) increases the MFM signal (greater frequency shift). Alternatively, susceptibility contrast can be confirmed by observing a difference between MFM images obtained with oppositely magnetized tips, provided that the creation of each image does not cause irreversible changes;[1] even if no irreversible changes are apparent while scanning, irreversible changes should be ruled out by performing consecutive MFM scans with tip magnetized in the same direction.

A key advantage of susceptibility contrast is that it can be used to observe magnetic objects that are smaller than the

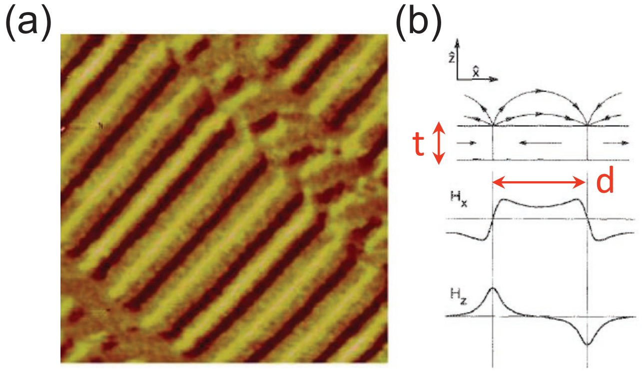

Figure 20. Charge contrast. a) 40 µm × 40 µm MFM image of a hard disc showing diagonal tracks in which IP domains (intermediate contrast) are separated by domain walls (bright and dark contrast). b) Head-to-head and tail-to-tail domain walls generate vertical stray-field components H_z of opposite sign, such that the detected quantity $\partial^2 H_z/\partial z^2$ takes values of opposite sign. b) Reproduced with permission.[46] Copyright 1990, IOP Publishing.

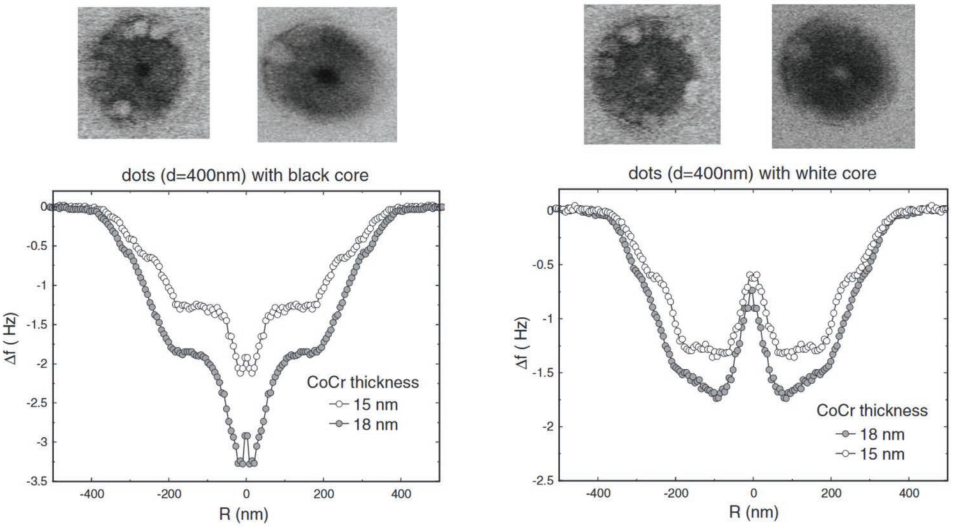

Figure 21. Susceptibility contrast. Magnetic vortices in permalloy discs appear dark in MFM because they are modified by a CoCr tip to which they are attracted. The thicker the magnetic coating of the tip, the greater the attraction, and hence the greater the measured frequency shift. The two images and the cross-section on the left (right) represent a vortex whose core is magnetized parallel (antiparallel) to the tip magnetization. Reproduced with permission.[47] Copyright 2004, IOP Publishing.

spatial resolution of MFM. Importantly, such observations can be made even when the tip-sample interactions are not strong enough to irreversibly modify the object under study. For example, susceptibility contrast has been used to image vortex cores[48] that are unswitched by the imaging (**Figure 22**); the diameters of these vortex cores are independently known to be ≤10 nm.[49]

8.3. Strong Interactions

The magnetic interactions between sample and tip are so strong that the tip is likely to induce irreversible magnetic changes in the sample, or vice versa, depending on the relative coercivities of tip and sample. Strong tip-sample interactions thus corrupt magnetic imaging (**Figure 23**).

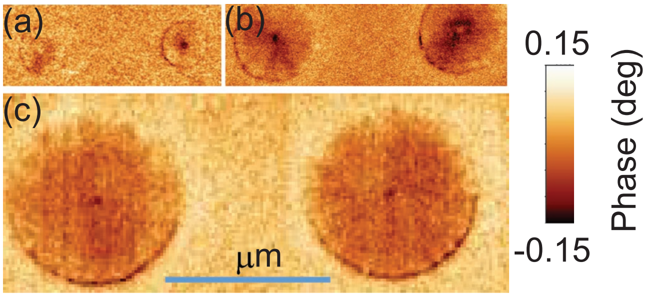

Figure 22. Susceptibility contrast for detection beyond the resolution limit. MFM images show magnetic vortices in 25 nm-thick permalloy discs of diameter a) 250 nm, b) 500 nm and c) 1 µm. Vortex cores that appear dark (less dark) are magnetized antiparallel (parallel) to the moment of the MFM tip.

9. Comparison and Contextualization of XPEEM and MFM

We have seen that XPEEM can be used to image both different types of magnetism and ferroelectricity by using the appropriate contrast mechanism (XMCD or XLD). Moreover, the contrast mechanism can be changed without changing the control parameters of the sample (temperature, applied electric field,

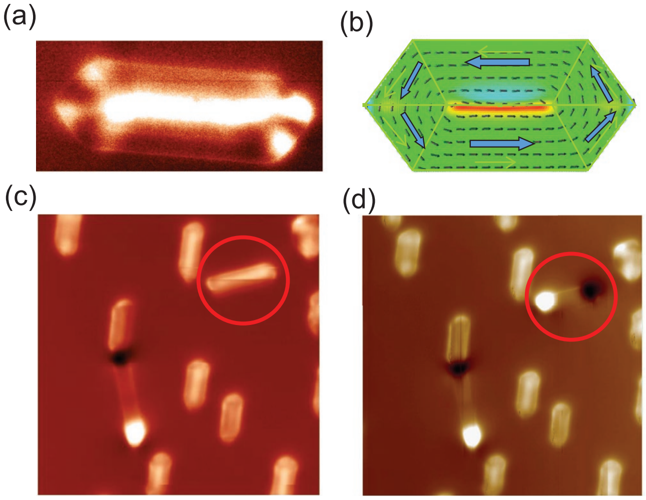

Figure 23. Susceptibility contrast versus strong tip-sample interactions. The figure describes self-assembled Fe (110) dots of length ≈2.5 µm.[50] Flux-closure domains are a) resolved using susceptibility contrast and b) predicted via micromagnetic simulation (reproduced with permission from O. Fruchart). c) No flux-closure domains are observed when tip-sample interactions are strong. d) Even stronger tip-sample interactions irreversibly switch the circled dot into a single-domain state. For simplicity, we have omitted the MFM color scales in (a,c,d), and the color scale for the OOP component of magnetization in (b).

Table 1. Summary of key magnetic imaging techniques. The benchtop, facility, and highly specialized techniques populate pixels via parallel acquisition or scanning. The possibilities of acquiring quantitative and time-resolved data are identified via Y (yes) and N (no). Resolutions under standard conditions are given without parentheses, ultimate resolutions under special conditions are given with parentheses. Contrast mechanisms are described using the following abbreviations: SP = spin-polarized, **M** = magnetization, **B** = magnetic flux density. TEM = transmission electron microscopy. SPLEEM = spin polarized low energy electron microscopy. SEMPA = scanning electron microscopy with polarization analysis. MexFM = magnetic exchange force microscopy. SP STM = spin-polarized scanning tunnelling microscopy.

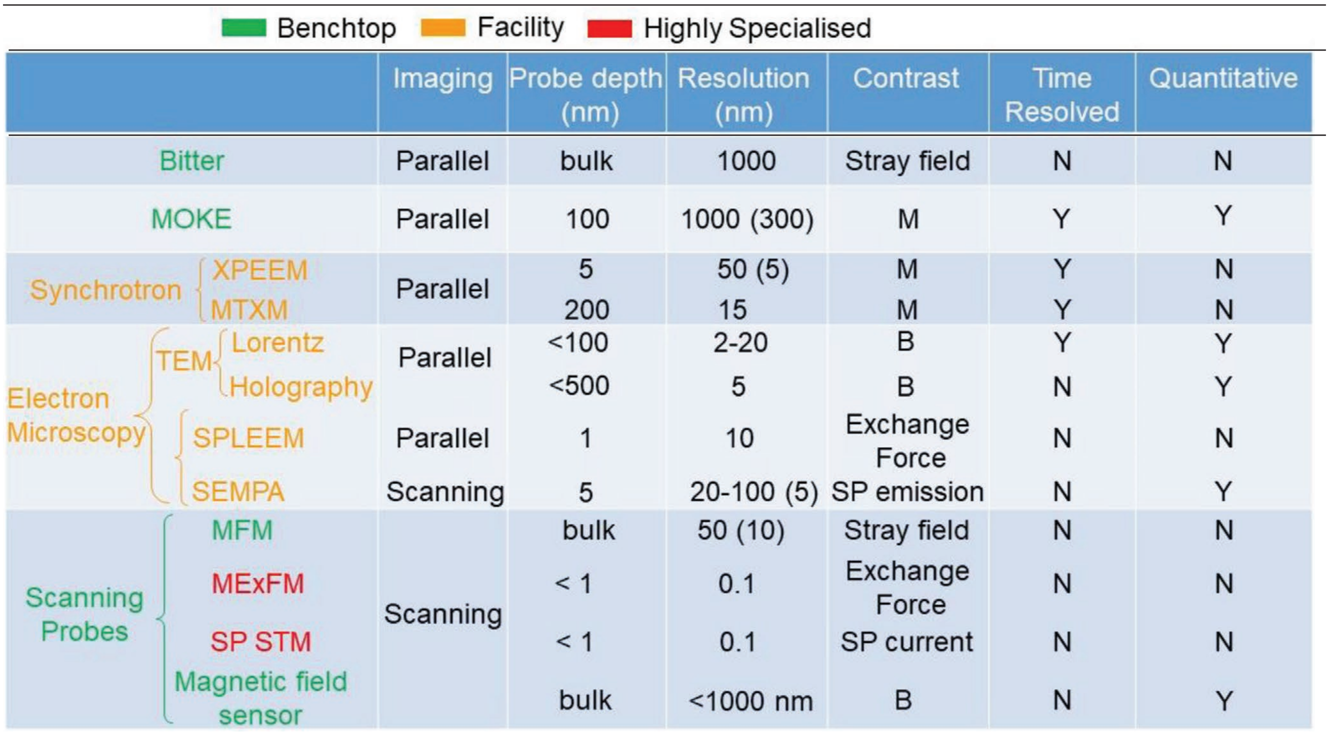

🟩 Benchtop 🟧 Facility 🟥 Highly Specialised

		Imaging	Probe depth (nm)	Resolution (nm)	Contrast	Time Resolved	Quantitative
Bitter		Parallel	bulk	1000	Stray field	N	N
MOKE		Parallel	100	1000 (300)	M	Y	Y
Synchrotron	XPEEM	Parallel	5	50 (5)	M	Y	N
	MTXM		200	15	M	Y	N
Electron Microscopy	TEM Lorentz	Parallel	<100	2-20	B	Y	Y
	TEM Holography		<500	5	B	N	Y
	SPLEEM	Parallel	1	10	Exchange Force	N	N
	SEMPA	Scanning	5	20-100 (5)	SP emission	N	Y
Scanning Probes	MFM	Scanning	bulk	50 (10)	Stray field	N	N
	MExFM		< 1	0.1	Exchange Force	N	N
	SP STM		< 1	0.1	SP current	N	N
	Magnetic field sensor		bulk	<1000 nm	B	N	Y

applied magnetic field, current injection). Analogously, magnetic imaging with MFM can be complemented by using piezoforce microscopy (PFM) to image ferroelectric domains, as the vector polarization influences the phase of the piezoresponse that is locally driven in the sample between the tip and a back electrode.[51,52] However, switching between MFM and PFM requires a change of tip that is liable to preclude holding set control parameters constant. For example, if measuring away from room temperature then one would expect to return to room temperature before opening the system and changing the tip.

XPEEM and MFM/PFM both offer similarly high spatial resolutions that permit ferroic domain processes to be imaged in good detail (typically 50 nm, at best 10 nm,[20,21]), and neither technique requires complex sample preparation. Key ways in which the two techniques differ are as follows. Unlike MFM, XPEEM can probe both IP and OOP components of magnetization if the incident X-ray beam is not normal to the surface, permitting the construction of vector maps of IP magnetization (Section 7.1.2.). Unlike MFM, XPEEM can image antiferromagnetic domains (Section 7.2.4.). Unlike MFM, XPEEM data cannot be corrupted by dipolar tip-sample interactions. Unlike XPEEM, MFM is a relatively cheap benchtop technique that is widely available, while XPEEM requires large facilities at which access is competitive. Unlike XPEEM, MFM can image buried layers that are tens of nanometres deep, although XPEEM images represent the more precise probe depth of ≈5 nm.

We close this section by setting XPEEM and MFM in the context of other techniques for magnetic imaging (**Table 1**). These techniques range from the first reported images of magnetic domains[53,54] (**Figure 24**a) to the detection of magnetic moments on individual atoms[55] (Figure 24b).

10. XMCD-PEEM and MFM Images of Magnetism under Electrical Control

The first magnetoelectric effect to be experimentally demonstrated (in Cr_2O_3[56]) was a direct magnetoelectric effect, in which applied a magnetic field modified the electrical polarization. However, the magnetoelectric renaissance that began in the early 2000s[57–59] has involved much research on converse magnetoelectric effects, in which an electric field modifies the magnetism in either the same material, or a juxtaposed material. The electrically driven magnetic changes can be spatially complex, for example, when ferromagnetic domains undergo switching, so imaging is highly desirable. Ideally, one should also image the polar order that

Table 2. Magnetoelectric device parameters. Four magnetoelectric coupling mechanisms (cartoons at top) are compared in terms of the performance they might yield when employed in low-power memory devices. In all cases, data are written into the magnetic layer (blue) by electrically addressing the juxtaposed layer (orange), and the state of the magnetic layer can then be read, for example, via the electrical resistance of a magnetic tunnel junction in which it forms the free layer.[62,67] The references cited on the bottom line are cited in our main text for each of the four effects. Reproduced with permission.[68] Copyright 2019, AIP Publishing LLC.

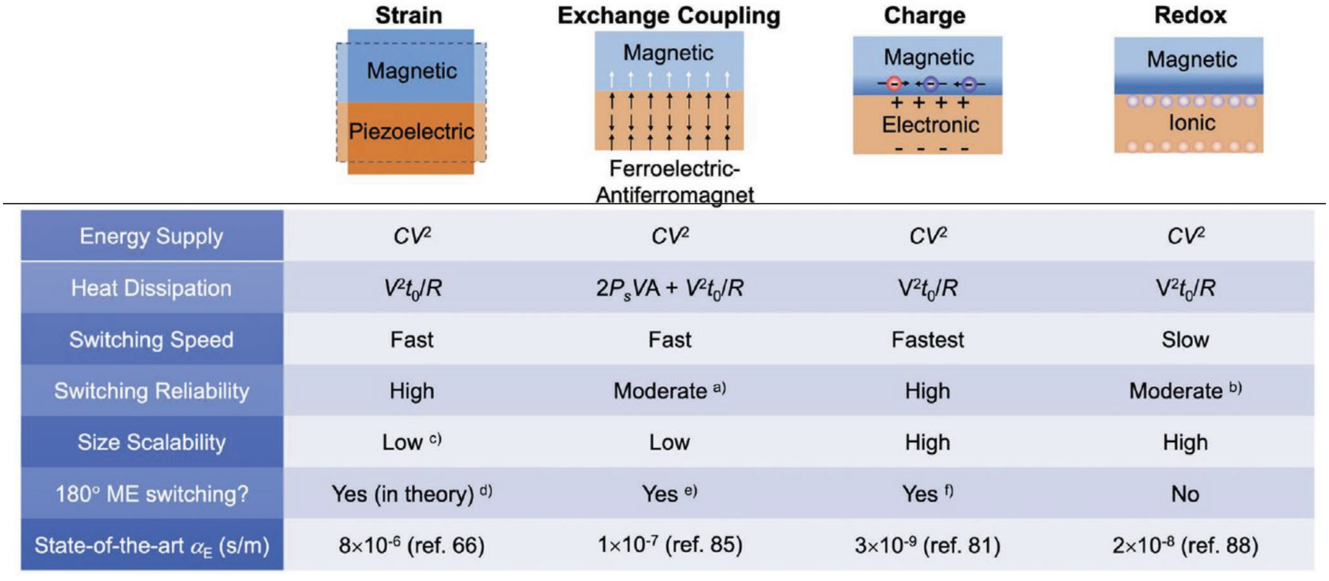

	Strain	Exchange Coupling	Charge	Redox
Energy Supply	CV^2	CV^2	CV^2	CV^2
Heat Dissipation	V^2t_0/R	$2P_sVA + V^2t_0/R$	V^2t_0/R	V^2t_0/R
Switching Speed	Fast	Fast	Fastest	Slow
Switching Reliability	High	Moderate [a)]	High	Moderate [b)]
Size Scalability	Low [c)]	Low	High	High
180° ME switching?	Yes (in theory) [d)]	Yes [e)]	Yes [f)]	No
State-of-the-art α_E (s/m)	8×10^{-6} (ref. 66)	1×10^{-7} (ref. 85)	3×10^{-9} (ref. 81)	2×10^{-8} (ref. 88)

drives the magnetic changes in order to identify the degree of correlation.

Converse magnetoelectric effects are parameterized via coupling parameter $\alpha = \mu_0 \mathrm{d}M/\mathrm{d}E$, and the values of this parameter are small in single-phase materials (μ_0 is the permeability of free space, M is the volume-normalized magnetization of the magnetic phase, and E is the applied electric field). For example, in Cr_2O_3 ($\alpha = 4.1 \times 10^{-12}$ sm^{-1},[56]) and $TbPO_4$ ($\alpha = 36.7 \times 10^{-12}$ sm^{-1},[60]), the applied electric field is assumed to have little influence on the antiferromagnetic order. The coupling parameter is not large even when antiferromagnetic domains are known to have been switched by the electrically driven switching of ferroelectric domains, as seen in the most widely studied single-phase multiferroic ($BiFeO_3$, BFO),[61] but this magnetoelectric switching can nevertheless be used to switch the magnetization of a juxtaposed ferromagnet via strain and/or exchange bias.[62,63] By thus combining an electrically addressed ferroelectric with a juxtaposed ferromagnetic film, one may obtain coupling parameters that are many orders of magnitude larger than the aforementioned values for monolithic materials, for example, $\alpha = 8.0 \times 10^{-6}$ s m^{-1} for a polycrystalline CoFeB film that is strain coupled to its single-crystal substrate of PMN-PT.[64] This coupling parameter currently represents the record value for converse magnetoelectric effects that are repeatable, and it is presented in **Table 2** together with similar coupling parameters that are mediated by exchange

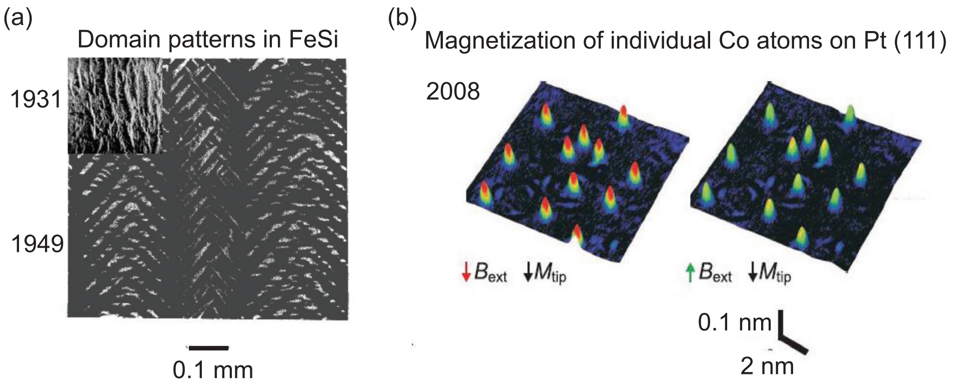

Figure 24. Progress in magnetic imaging. a) First reports of magnetic imaging in 1931 and 1949. The magnetic microstructures in FeSi alloys were observed using the Bitter decoration method. Reproduced with permission.[53] Copyright 1931, American Physical Society. Reproduced with permission.[54] Copyright 1949, American Physical Society. b) Detection of individual magnetic moments in 2008. Data for separated Co atoms were obtained using spin-polarized scanning tunneling microscopy (SPSTM). Reproduced with permission.[55] Copyright 2008, AAAS.

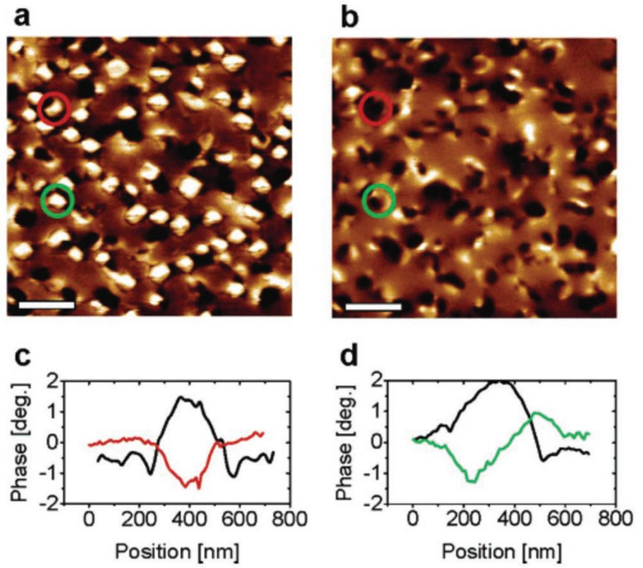

Figure 25. Voltage-driven magnetization reversal in sub-micron nanopillars of ferrimagnetic $CoFe_2O_4$. a,b) MFM images of a $(BiFeO_3)_{0.65}$-$(CoFe_2O_4)_{0.35}$ composite film are shown a) at magnetic remanence after saturating in an OOP magnetic field, and b) after subsequently applying 12 V between the scanned tip and a bottom electrode. This voltage poles the $BiFeO_3$ matrix, and can thus modify the $CoFe_2O_4$ magnetization via exchange coupling. Scale bars are 1 µm. c) For the $CoFe_2O_4$ pillar circled red in (a,b), line profiles show cross-sections before (black) and after (red). d) For the $CoFe_2O_4$ pillar circled green in (a,b), line profiles show cross-sections before (black) and after (green). Reproduced with permission.[69] Copyright 2005, American Chemical Society.

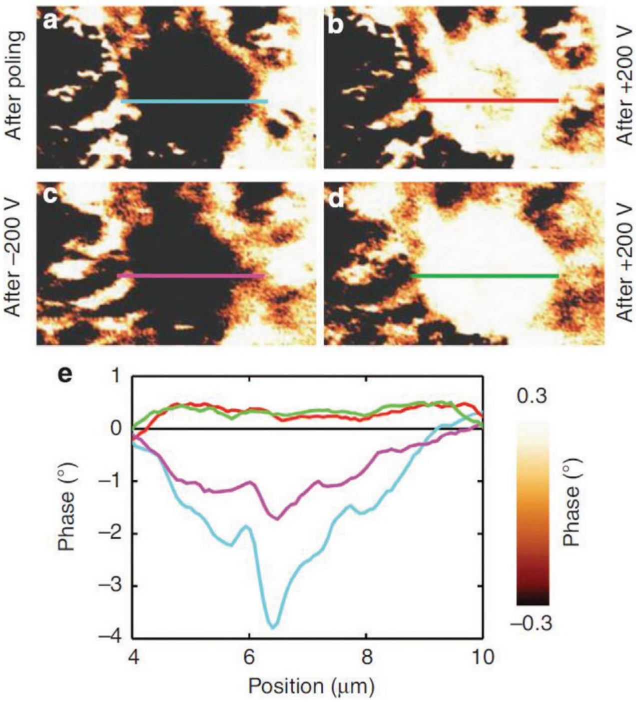

Figure 26. Voltage-driven magnetization reversal in the Ni electrode of a multilayer capacitor. (a-d) 12 µm × 7 µm MFM images showing part of a Ni electrode that was brought near surface by polishing a BTO-based multilayer capacitor (KEMET 1210). The images were obtained with no voltage applied across the MLC terminals after applying and removing voltages of a) −200 V b) +200 V, c) −200 V and d) +200 V. e) Color-coded cross-sections show large phase shifts (cf. 2° for domains in commercial videotape). Although counterintuitive, the asymmetry implies complete magnetization reversal in the disc-shaped feature, as imaging such a feature with the tip magnetization first up and then down yields a similar asymmetry (Figure 2 of ref. [61]). Reproduced with permission.[70] Copyright 2013, Springer Nature.

coupling,[62] charge coupling,[65] and redox processes.[66] More generally, Table 2 is a summary of parameters that are relevant for exploiting converse magnetoelectric effects in memory devices.

Converse magnetoelectric effects were rarely imaged until recently, and yet imaging has revealed details that cannot be resolved in macroscopic measurements, as may be appreciated from the images shown in this paper. Of particular interest are voltage-driven magnetization reversals, which arise at specific locations (**Figures 25–27**),[63,69,70] and which in their purest form should be symmetry forbidden given that a spatial change should not yield a change that would arise purely from time-reversal (time-reversal implies magnetization reversal).

11. Summary and Future Work

We and others habitually use XPEEM and MFM to image complex magnetic and polar order in magnetic and ferroelectric materials, most notably when studying magnetoelectric phenomena. The examples we present show that these images provide not only beauty, but also key insights that elude macroscopic measurement.

Both XPEEM and MFM achieve sub-micron spatial resolutions (typically 50 nm, at best 10 nm,[20,21]). Both techniques permit complementary imaging modes that permit the observation of ferromagnetic order (XMCD contrast and MFM), antiferromagnetic order (XMLD contrast not MFM), and ferroelectric order (XNLD contrast and PFM). Both techniques can be performed while varying an applied electric field, varying an applied magnetic field, varying temperature, and injecting current. XPEEM outperforms MFM because it directly maps order parameters, and these can be presented on vector maps. However, MFM outperforms XPEEM in terms of ease of access, cost, and probe depth.

In future, XPEEM with aberration-corrected microscopes will become more widespread, as should access to lower temperatures. Equipment developments of this type will be particularly important for resolving ever finer features in ever thinner samples, for example, skyrmions and 2D materials. Moreover, it should become possible to perform 3D magnetic mappings with XMCD-PEEM, either by obtaining data for multiple IP orientations of the sample (rather than the two orthogonal IP orientations used for vector maps), or by combining XMCD-PEEM data with MFM data. The future of imaging therefore looks clear, cool, 3D, and bright.

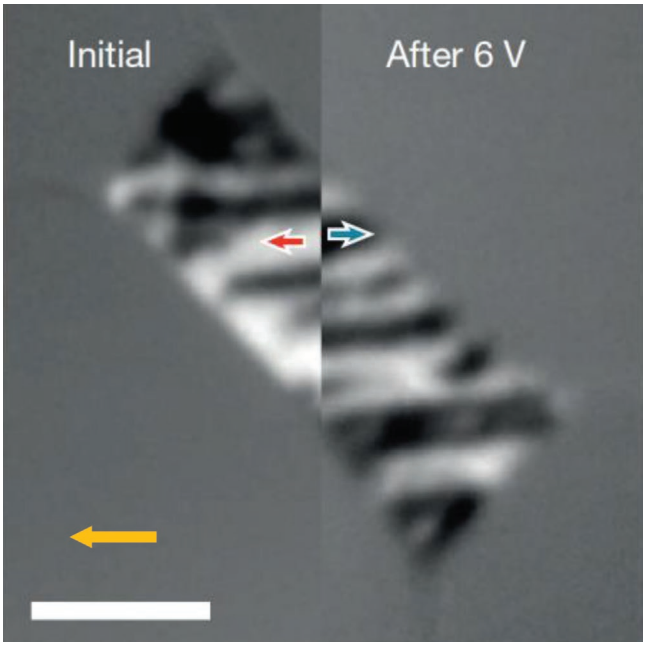

Figure 27. Voltage-driven magnetization reversal in a CoFe island. Using data from two XMCD-PEEM images, part of the island is shown in its initial state, while the other part is shown after applying and removing 6 V across an underlying epitaxial film of BFO. Magnetization directions (red and blue arrows) are collinear with the IP projection of the X-ray beam (orange arrow). The voltage appears to reverse the local magnetization at some locations due to exchange coupling between the island and the clamped BFO. Scale bar is 2 µm. Reproduced with permission.[63] Copyright 2014, Springer Nature.

Acknowledgements

The authors thank R. Mansell for fabricating the samples described in Figures 10 and 22. The authors thank O. Fruchart for providing the sample described in Figure 23. The authors thank D. Pesquera, B. Nair, J. Wang, and S. Kurdi for helping to collect the data presented in Figure 10. Funding that supported the unpublished parts of this work was provided by Isaac Newton Trust grants 10.26(u) and 11.35(u), and UK EPSRC grant EP/G031509/1. The authors acknowledge Diamond Light Source for time on I06 under proposals SI19060 and MM22255.

Conflict of Interest

The authors declare no conflict of interest.

Keywords

magnetic imaging, magnetoelectrics, multiferroics

Received: February 14, 2022
Revised: May 15, 2022

---

[1] A. Hubert, R. Schäfer, *Magnetic Domains: The Analysis of Magnetic Microstructures*, Springer, Berlin **2009**.
[2] L. W. Martin, A. M. Rappe, *Nat. Rev. Mater.* **2016**, *2*, 16087.
[3] J.-M. Hu, Z. Li, L. Q. Chen, C. W. Nan, *Nat. Commun.* **2011**, *2*, 553.
[4] F. Matsukura, Y. Tokura, H. Ohno, *Nat. Nanotechnol.* **2015**, *10*, 209.
[5] G. Catalan, J. Seidel, R. Ramesh, J. F. Scott, *Rev. Mod. Phys.* **2012**, *84*, 119.
[6] D. Viehland, E. K. H. Salje, *Adv. Phys.* **2014**, *63*, 267.
[7] L. Pierobon, A. Kovács, R. E. Schäublin, S. S. A. Gerstl, J. Caron, U. V. Wyss, R. E. Dunin-Borkowski, J. F. Löffler, M. Charilaou, *Sci. Rep.* **2020**, *10*, 21209.
[8] P. W. Forsbergh Jr., *Phys. Rev.* **1949**, *76*, 1187.
[9] M. Staňo, O. Fruchart, *Handbook of Magnetic Materials*, Vol. *27*, Elsevier, Amsterdam **2018**, Ch. 3, p. 155.
[10] J. Sampaio, V. Cros, S. Rohart, A. Thiaville, A. Fert, *Nat. Nanotechnol.* **2013**, *8*, 839.
[11] A. Fert, N. Reyren, V. Cros, *Nat. Rev. Mater.* **2017**, *2*, 17031.
[12] K. Yamada, S. Kasai, Y. Nakatani, K. Kobayashi, H. Kohno, A. Thiaville, T. Ono, *Nat. Mater.* **2007**, *6*, 270.
[13] A. K. Yadav, C. T. Nelson, S. L. Hsu, Z. Hong, J. D. Clarkson, C. M. Schlepütz, A. R. Damodaran, P. Shafer, E. Arenholz, L. R. Dedon, D. Chen, A. Vishwanath, A. M. Minor, L. Q. Chen, J. F. Scott, L. W. Martin, R. Ramesh, *Nature* **2016**, *530*, 198.
[14] D. Rusu, J. J. P. Peters, T. P. A. Hase, J. A. Gott, G. A. A. Nisbet, J. Strempfer, D. Haskel, S. D. Seddon, R. Beanland, A. M. Sanchez, M. Alexe, *Nature* **2022**, *602*, 240.
[15] A. Soumyanarayanan, N. Reyren, A. Fert, C. Panagopoulos, *Nature* **2016**, *539*, 509.
[16] Z. Hou, Y. Wang, X. Lan, S. Li, X. Wan, F. Meng, Y. Hu, Z. Fan, C. Feng, M. Qin, M. Zeng, X. Zhang, X. Liu, X. Fu, G. Yu, G. Zhou, Y. Zhou, W. Zhao, X. Gao, J. -. M. Liu, *Adv. Mater.* **2022**, *34*, 2107908.
[17] C. M. Schneider, G. Schonhense, *Rep. Prog. Phys.* **2002**, *65*, R1785.
[18] J. Stöhr, H. C. Siegmann, *Magnetism: From Fundamentals to Nanoscale Dynamics*, Springer, Berlin **2006**.
[19] O. Kazakova, R. Puttock, C. Barton, H. Corte-León, M. Jaafar, V. Neu, A. Asenjo, *J. Appl. Phys.* **2019**, *125*, 060901.
[20] A. Schwarz, R. Wiesendanger, *Nano Today* **2008**, *3*, 28.
[21] A. Locatelli, E. Bauer, *J. Phys.: Condens. Matter* **2008**, *20*, 093002.
[22] J. Stöhr, S. Anders, *IBM J. Res. Dev.* **2000**, *44*, 535.
[23] M. Ghidini, R. Mansell, F. Maccherozzi, X. Moya, L. C. Phillips, W. Yan, D. Pesquera, C. H. W. Barnes, R. P. Cowburn, J.-M. Hu, S. S. Dhesi, N. D. Mathur, *Nat. Mater.* **2019**, *18*, 840.
[24] S. V. Kalinin, D. A. Bonnell, *Phys. Rev. B* **2001**, *63*, 125411.
[25] A. Hofer, M. Fechner, K. Duncker, M. Hölzer, I. Mertig, W. Widdra, *Phys. Rev. Lett.* **2012**, *108*, 087602.
[26] W. G. Stirling, M. J. Cooper, *J. Magn. Magn. Mater.* **1999**, *200*, 755.
[27] E. Stern, *J. Synchrotron Radiat.* **2001**, *8*, 49.
[28] D. Attwood, *Soft X-Rays and Extreme Ultraviolet Radiation, Principle and Applications*, Cambridge University Press, Cambridge **1999**.
[29] M. Ghidini, R. Mansell, R. Pellicelli, D. Pesquera, B. Nair, X. Moya, S. Farokhipoor, F. Maccherozzi, C. H. W. Barnes, R. P. Cowburn, S. S. Dhesi, N. D. Mathur, *Nanoscale* **2020**, *12*, 5652.
[30] L. E. Hueso, J. M. Pruneda, V. Ferrari, G. Burnell, J. P. Valdés-Herrera, B. D. Simons, P. B. Littlewood, E. Artacho, A. Fert, N. D. Mathur, *Nature* **2007**, *445*, 410.
[31] A. Scholl, H. Ohldag, F. Nolting, J. Stöhr, H. Padmore, *Rev. Sci. Instrum.* **2002**, *73*, 1362.
[32] J. Rhensius, C. A. F. Vaz, A. Bisig, S. Schweitzer, J. Heidler, H. S. Körner, A. Locatelli, M. A. Niño, M. Weigand, L. Méchin, F. Gaucher, E. Goering, L. J. Heyderman, M. Kläui, *Appl. Phys. Lett.* **2011**, *99*, 062508.
[33] M. Ghidini, F. Maccherozzi, X. Moya, L. C. Phillips, W. Yan, J. Soussi, N. Métallier, M. E. Vickers, N.-J. Steinke, R. Mansell, C. H. W. Barnes, S. S. Dhesi, N. D. Mathur, *Adv. Mater.* **2015**, *27*, 1460.
[34] D. Pesquera, E. Khestanova, M. Ghidini, S. Zhang, A. P. Rooney, F. Maccherozzi, P. Riego, S. Farokhipoor, J. Kim, X. Moya, M. E. Vickers, N. A. Stelmashenko, S. J. Haigh, S. S. Dhesi, N. D. Mathur, *Nat. Commun.* **2020**, *11*, 3190.

[35] X. Moya, L. E. Hueso, F. Maccherozzi, A. I. Tovstolytkin, D. I. Podyalovskii, C. Ducati, L. C. Phillips, M. Ghidini, O. Hovorka, A. Berger, M. E. Vickers, E. Defay, S. S. Dhesi, N. D. Mathur, *Nat. Mater.* **2013**, *12*, 52.
[36] E. Arenholtz, G. Van Der Laan, A. Fraile-Rodríguez, P. Yu, Q. He, R. Ramesh, *Phys. Rev. B* **2010**, *82*, 140103.
[37] J. Stöhr, *NEXAFS Spectroscopy*, Springer, Berlin Heidelberg **1992**.
[38] R. V. Chopdekar, V. K. Malik, A. Fraile Rodríguez, L. Le Guyader, Y. Takamura, A. Scholl, D. Stender, C. W. Schneider, C. Bernhard, F. Nolting, L. J. Heyderman, *Phys. Rev. B* **2012**, *86*, 014408.
[39] M. Ghidini, B. Zhu, R. Mansell, R. Pellicelli, A. Lesaine, X. Moya, S. Crossley, B. Nair, F. Maccherozzi, C. H. W. Barnes, R. P. Cowburn, S. S. Dhesi, N. D. Mathur, *J. Phys. D: Appl. Phys.* **2018**, *51*, 224007.
[40] M. Ghidini, R. Pellicelli, R. Mansell, D. Pesquera, B. Nair, X. Moya, S. Farokhipoor, F. Maccherozzi, C. H. W. Barnes, R. P. Cowburn, S. S. Dhesi, N. D. Mathur, *J. Phys. D: Appl. Phys.* **2020**, *53*, 434003.
[41] M. M. Schwickert, G. Y. Guo, M. A. Tomaz, W. L. O'Brien, G. R. Harp, *Phys. Rev. B* **1998**, *58*, R4289(R).
[42] J. Lüning, F. Nolting, A. Scholl, H. Ohldag, J. W. Seo, J. Fompeyrine, J.-P. Locquet, J. Stöhr, *Phys. Rev. B* **2003**, *67*, 214433.
[43] E. Arenholz, G. van der Laan, R. V. Chopdekar, Y. Suzuki, *Phys. Rev. B* **2006**, *74*, 094407.
[44] F. Nolting, A. Scholl, J. Stöhr, J. W. Seo, J. Fompeyrine, H. Siegwart, J.-P. Locquet, S. Anders, J. Lüning, E. E. Fullerton, M. F. Toney, M. R. Scheinfein, H. A. Padmore, *Nature* **2000**, *405*, 767.
[45] F. P. Chmiel, N. Waterfield Price, R. D. Johnson, A. D. Lamirand, J. Schad, G. Van Der Laan, D. T. Harris, J. Irwin, M. S. Rzchowski, C.-B. Eom, P. G. Radaelli, *Nat. Mater.* **2018**, *17*, 581.
[46] D. Rugar, H. J. Mamin, P. Guethner, S. E. Lambert, J. E. Stern, I. Mcfadyen, T. Yogi, *J. Appl. Phys.* **1990**, *68*, 1169.
[47] J. M. Garcia-Martin, A. Thiaville, J. Miltat, T. Okuno, L. Vila, L. Piraux, *J. Phys. D: Appl. Phys.* **2004**, *37*, 965.
[48] T. Shinjo, T. Okuno, R. Hassdorf, K. Shigeto, T. Ono, *Science* **2000**, *289*, 930.
[49] A. Wachowiak, J. Wiebe, M. Bode, O. Pietzsch, M. Morgenstern, R. Wiesendanger, *Science* **2002**, *298*, 577.
[50] O. Fruchart, P. O. Jubert, M. Eleoui, F. Cheynis, B. Borca, P. David, V. Santonacci, A. Liénard, M. Hasegawa, C. Meyer, *J. Phys.: Condens. Matter* **2007**, *19*, 053001.
[51] N. Balke, I. Bdikin, S. V. Kalinin, A. L. Kholkin, *J. Am. Ceram. Soc.* **2009**, *92*, 1629.
[52] S. Kalinin, A. N. Morozovska, L. Q. Chen, B. J. Rodriguez, *Rep. Prog. Phys.* **2010**, *73*, 056502.
[53] F. Bitter, *Phys. Rev.* **1931**, *38*, 1903.
[54] H. J. Williams, R. M. Bozorth, W. Shockley, *Phys. Rev.* **1949**, *75*, 155.
[55] F. Meier, L. Zhou, J. Wiebe, R. Wiesendanger, *Science* **2008**, *320*, 82.
[56] D. N. Astrov, *J. Exp. Theor. Phys.* **1961**, *13*, 729.
[57] M. Fiebig, *J. Phys. D: Appl. Phys.* **2005**, *38*, R123.
[58] W. Eerenstein, J. F. Scott, N. D. Mathur, *Nature* **2006**, *442*, 759.
[59] N. A. Spaldin, R. Ramesh, *Nat. Mater.* **2019**, *18*, 203.
[60] G. T. Rado, J. M. Ferrari, W. G. Maisch, *Phys. Rev. B* **1984**, *29*, 4041.
[61] D. Lebeugle, A. Mougin, M. Viret, D. Colson, L. Ranno, *Phys. Rev. Lett.* **2009**, *103*, 257601.
[62] N. D. Mathur, *Nature* **2008**, *591*, 454.
[63] J. Heron, J. L. Bosse, Q. He, Y. Gao, M. Trassin, L. Ye, J. D. Clarkson, C. Wang, J. Liu, S. Salahuddin, D. C. Ralph, D. G. Schlom, J. Íñiguez, B. D. Huey, R. Ramesh, *Nature* **2014**, *516*, 370.
[64] J. Wang, D. Pesquera, R. Mansell, S. Van Dijken, R. P. Cowburn, M. Ghidini, N. D. Mathur, *Appl. Phys. Lett.* **2019**, *114*, 092401.
[65] D. Chiba, S. Fukami, K. Shimamura, N. Ishiwata, K. Kobayashi, T. Ono, *Nat. Mater.* **2011**, *10*, 853.
[66] C. Bi, Y. Liu, T. Newhouse-Illige, M. Xu, M. Rosales, J. W. Freeland, O. Mryasov, S. Zhang, S. G. E. Te Velthuis, W. G. Wang, *Phys. Rev. Lett.* **2014**, *113*, 267202.
[67] M. Bibes, A. Barthélémy, *Nat. Mater.* **2008**, *7*, 425.
[68] J. Hu, C.-W. Nan, *APL Mater.* **2019**, *7*, 080905.
[69] F. Zavaliche, H. Zheng, L. Mohaddes-Ardabili, S. Y. Yang, Q. Zhan, P. Shafer, E. Reilly, R. Chopdekar, Y. Jia, P. Wright, D. G. Schlom, Y. Suzuki, R. Ramesh, *Nano Lett.* **2005**, *5*, 1793.
[70] M. Ghidini, R. Pellicelli, J. L. Prieto, X. Moya, J. Soussi, J. Briscoe, S. Dunn, N. D. Mathur, *Nat. Commun.* **2013**, *4*, 1453.